nanomaterials

MDPI

Article

Photoluminescence of Rhodamine from Nano-Confinement Inside 3D Sculptured Coatings

Lina Grineviciute [1,2,*,†], Hsin-Hui Huang [3,4,5,*,†], Haoran Mu [3,5], William McMahon-Puce [3], James W. M. Chon [3], Saulius Juodkazis [2,3,5] and Andrew H. A. Clayton [3]

1 Center for Physical Sciences and Technology, Savanoriu Ave. 231, LT-02300 Vilnius, Lithuania
2 Laser Research Center, Physics Faculty, Vilnius University, Saulėtekio Ave. 10, LT-10223 Vilnius, Lithuania; sjuodkazis@swin.edu.au
3 Optical Sciences Centre, Swinburne University of Technology, Hawthorn, VIC 3122, Australia; haoranmu@swin.edu.au (H.M.); wmcmahonpuce@swin.edu.au (W.M.-P.); jchon@swin.edu.au (J.W.M.C.); aclayton@swin.edu.au (A.H.A.C.)
4 Australian Research Council (ARC) Industrial Transformation Training Centre in Surface Engineering for Advanced Materials (SEAM), Swinburne University of Technology, Hawthorn, VIC 3122, Australia
5 Melbourne Centre for Nanofabrication (MCN), 151 Wellington Road, Clayton, VIC 3168, Australia
* Correspondence: lina.grineviciute@ftmc.lt (L.G.); hsinhuihuang@swin.edu.au (H.-H.H.)
† These authors contributed equally to this work.

Abstract

The effect of the confinement of fluorophores (rhodamine 6G) in nano-cavities of porous 3D sculptured coatings made by glancing-angle deposition (GLAD) was investigated by fluorescence-lifetime imaging microscopy (FLIM). Shortening of fluorescence/photoluminescence lifetime by ∼10% was observed from the dye-permeated (in liquid) structure; however, there was no rotational hindrance of dye molecules. When dried, a strong rotational hindrance 89% was observed for the orientation along the ordinary optical axis (slow-axis), and the hindrance was smaller than 57% for the extraordinary direction (fast axis). Light-intensity distribution inside the nano-structure with a form birefringence was numerically modeled using plane-wave illumination and a dipole source. Nanoscale localization of light intensity due to dipole nature $I \sim 1/radius^6$ and boundary conditions for E-field allows efficient energy deposition inside the region of lower refractive index (nanogaps).

Keywords: 3D sculptured coatings; glancing-angle deposition (GLAD); fluorescence-lifetime imaging microscopy (FLIM)

Academic Editor: Wojciech Pisarski

Received: 20 January 2026
Revised: 18 February 2026
Accepted: 21 February 2026
Published: 26 February 2026

1. Introduction

Birefringence and optical activity (birefringence for circularly polarized light) are useful material properties, which originate from the material structure defined at the molecular/atomic level. The same properties can be engineered via larger structural building blocks at the nanoscale, e.g., via 3D control of nanofilm coating using glancing-angle deposition (GLAD) [1,2]. The folding of growth by fast-change deposition angle and azimuthal rotation around the normal axis to the surface, 3D structures endowed with form birefringence, and optical activity can be formed [3]. Shadowing during film formation by GLAD also induces porosity [4,5], which becomes a key advantage for the performance of GLAD coatings under high-power laser irradiation, where rapid local heating occurs. Local rapid heating typically causes coating failure, and GLAD coatings exhibit higher tolerances under such extreme conditions due to their porosity. The GLAD

coatings can achieve highly controlled thicknesses comparable to the wavelength of light ~1 μm or thicker, which makes them suitable for polarization active functions such as waveplates $\lambda/2$, $\lambda/4$. Furthermore, zero-order waveplates can be made with micrometer-thick GLAD coatings with various isotropic materials, e.g., evaporated/sputtered SiO_2 [6,7]. Releasable micrometer-thin waveplates can be made from alumina on a Cu mirror surface for optomechanical applications [8]. Three-dimensional nanofilms can also find applications in spectral–spatial filtering applications due to strongly expressed Fano resonances [9,10], and they can be formed on nano-structured surfaces [11].

How porosity affects the stability of 3D sculptured GLAD coatings needs a better understanding. It has been previously shown that porous GLAD films do not have increased surface-defect absorption in the case of SiO_2 films as determined by synchrotron IR micro-spectroscopy [12]. Nanogaps of 10–20 nm in the GLAD coatings are formed during a fast folding of the angle of deposition [13]. These nanogaps lie between the nano-walls and extend through the entire height of the 3D coating, usually 1–2 μm thick. Apart from micro-optical and polarization optics applications, such 3D coatings can be used in photo-catalysis applications. In particular, LaF_3-graphene composite showed efficient water splitting and H_2 generation under UV illumination [14]. Different phases of water films in nano-confinement were predicted [15] while production of a well controlled structures with 3D nanogaps and nano-channels is in high demand for water desalination and filter applications [16,17].

To understand how nanogap porosity interacts with an aqueous film, rhodamine 6G (RhD6G) was chosen due to its high quantum yield [18–20], strong sensitivity of its fluorescence lifetime to the local environment, and well-characterized dipole orientation [21–23], making it an ideal dye for studying nanoscale interactions. Here, we investigate the orientational properties of RhD6G in aqueous solution under nano-confinement, when RhD6G enters between the nanoplanes of a form-birefringent LaF_3 micro-film deposited by GLAD, using fluorescence-lifetime imaging microscopy (FLIM). Light LaF_3 localization inside nanogaps of the structure was further analyzed with numerical modeling.

2. Experimental Section: Samples and Methods

2.1. Three-Dimensional Sculptured Micro-Film Coatings

Anisotropic sculptured coatings were fabricated using the serial bi-deposition technique, which involves periodic 180° rotation of the substrate around its normal axis. This approach produces vertically aligned, elliptical columnar structures, thereby inducing birefringence. The LaF_3 films with a thickness of 1 μm were deposited at 60° angle of inclination on two fused silica samples using thermal evaporation. One of the samples was additionally covered with a dense capping layer to close the open voids. More fabrication details can be found here [24]. Figure 1 shows scanning electron microscopy (SEM) images of LaF_3 films.

2.2. Method: Fluorescence-Lifetime Imaging Microscopy

Fluorescence-lifetime imaging microscopy (FLIM) was used to determine the influence of nano-porosity of 3D sculptured coating of LaF_3 on the lifetime of rhodamine 6G (RhD6G). Aqueous solution of RhD6G at low concentration 5×10^{-6} mol was used to avoid dimer formation. An automatic pipette was used to dispense a 20 μL drop of rhodamine solution onto the substrates. Excitation of RhD6G was made with an LED with emission centered at 470 nm (Figure 2a). For the 3D sculptured LaF_3 coatings, the ordinary axis (n_o) is defined to be the slow axis with a higher refractive index and corresponds to the 0° orientation (aligned with the column growth plane). The extraordinary axis (n_e) is the fast axis with

a lower refractive indexing corresponding to the 90° orientation (perpendicular to the column growth plane).

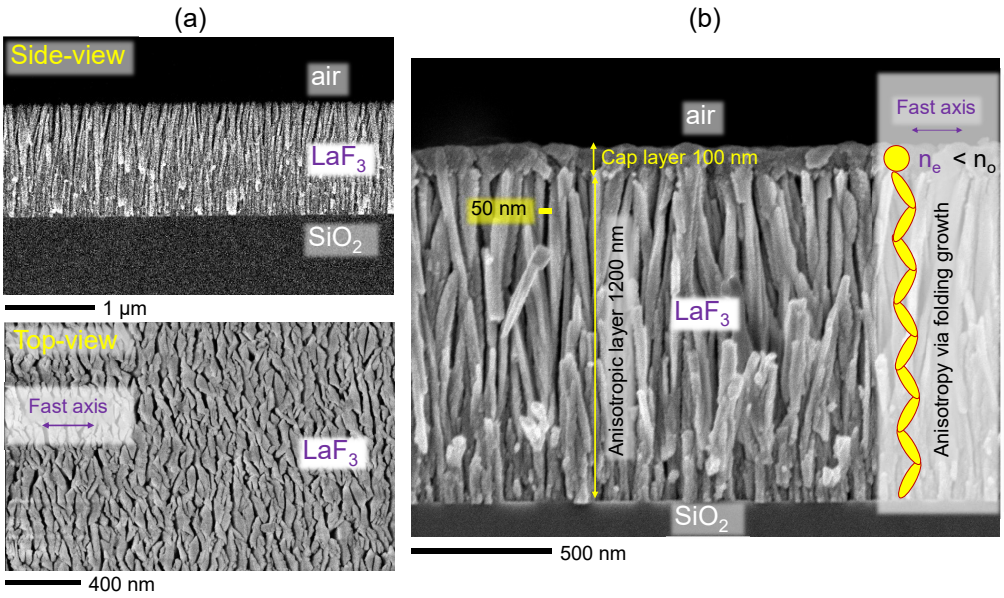

Figure 1. Samples. SEM images of LaF_3 3D sculptured film deposited by GLAD without (**a**) and with (**b**) cap layer. The structure is anisotropic and form-birefringent with $n_e < n_o$, where $n_{e,o}$ are the extraordinary and ordinary refractive indices, respectively, defined by the folding direction of the GLAD nano-structure; while the cap layer is isotropic and without porosity. The averaged refractive index of isotropic LaF_3 $n = 1.61$ at $\lambda = 470$ nm, which was used for excitation of RhD6G.

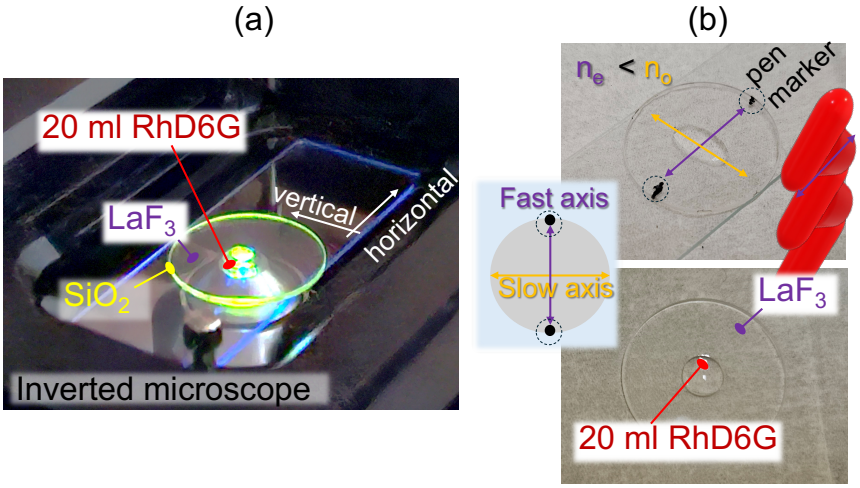

Figure 2. (**a**) Sample: 3D sculptured coating of LaF_3 (~1.2 μm thick) with 20 μL aqueous solution of rhodamine 6G (RhD6G) at concentration of 5×10^{-6} mol placed on FLIM microscope's stage and illuminated with laser emitting diode (LED) at 470 nm wavelength; fluorescence maximum is at 556 ± 10 nm (green). Orientations of the sample H, V along the horizontal and vertical axes of the sample stage are marked. Polarization of excitation was linear along the H-axis and was aligned with the slow (0°) or fast (90°) axis during FLIM measurements. (**b**) Samples with marked orientation of fast and slow axis ($n_e < n_o$, i.e., $fast < slow$). RhD6G solution is stretched along the slow axis on the uncapped coating (as Figure 1a) and forms an isotropic droplet spreading on the capped coating (as Figure 1b).

FLIM data acquisition and analysis were carried out with a commercial setup (LIFA, Lambert Instruments, Groningen, The Netherlands). The numerical aperture of the objective lens was $NA = 0.1$, wavelength of excitation $\lambda = 470$ nm. The diameter of the focus on the sample was $2w_0 = 1.22\lambda/NA = 5.7$ μm, and the depth of focus (DoF; double

the Rayleigh length) was $2z_R = 2\pi w_0^2/\lambda = 110$ µm. A sample, which was $d \simeq 1.2$ µm 3D sculptured porous LaF_3 film, was positioned at the optimized height inside DoF for maximum fluorescence.

FLIM allows the detection of spatial (orientation, translation) changes in emitting molecule, its transition dipole moment (TDM; Figure 3a) [25]. The molecule is excited along the selected orientation $\mathbf{n} \parallel \mathbf{X_1}$ with linearly polarized LED illumination, and two fluorescent intensities at cross-polarized orientations are measured $I_\parallel$ and $I_\perp$ (see Figure 3b). Excitation selects those dye molecules which have TDM aligned with polarization according to its projection $M_{TDM} \cos\theta$.

The second-rank order parameter for angle θ: $P_2(\theta) = [3\langle\cos^2\theta\rangle - 1]/2$, where $\langle \dots \rangle$ marks the average. By measuring fluorescence intensities at perpendicular and parallel polarizations with respect to the selected orientation (along $\mathbf{n} \parallel \mathbf{X_1}$), the second-order parameter P_2 or fluorescence anisotropy can be obtained:

$$P_2(\theta) = \frac{I_\parallel - I_\perp}{I_\parallel + 2I_\perp}. \tag{1}$$

Estimation of the molecule's (or chain's) second-order momentum P_2 is calculated by considering three angles between the measured transition dipole moment θ, the chain axis α_M and mutual orientation between polarization and chain φ (Figure 3a): $P_2(\theta) = P_2(\alpha_M) \times P_2(\varphi)$:

$$P_2(\varphi) \equiv \frac{P_2(\theta)}{P_2(\alpha_M)} = \frac{I_\parallel - I_\perp}{I_\parallel + 2I_\perp} \times \frac{2}{3\langle\cos^2\theta\rangle - 1}. \tag{2}$$

The TDM can be classified into two (parallel or perpendicular) anisotropies depending on the relation of φ to the magic angle 54.7° (the denominator is zero in Equation (2)). Notably, the same formalism described above for fluorescence applies to the absorption dichroism.

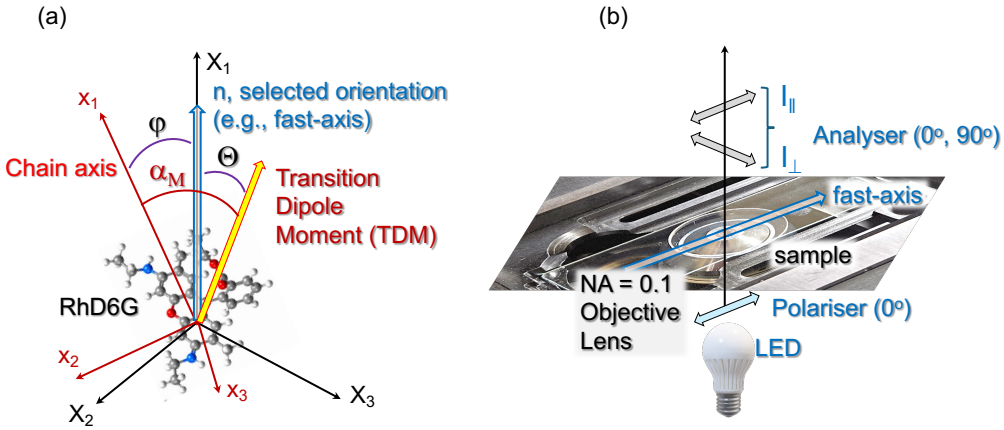

Figure 3. (**a**) Orientation of transition dipole moment (TDM) with respect to the selected direction, which is set to coincide with the X_1-axis of the coordinate system $X_1X_2X_3$. The orientation of molecular (or chain) direction is selected along the x_1-axis, where α_M is the orientation angle of the dipole. The angle φ defines the tilt between two coordinate systems. (**b**) FLIM methodology: polarized incident light excites fluorescence of selected (aligned) molecular dipoles, and emission is measured in two perpendicular orientations.

Anisotropy of the measured fluorescence intensity at two perpendicular orientations $I_{\parallel,\perp}$ is a fast-changing $r(t)$ when emitting objects are rotating and translating from the pre-selected orientation defined by the linear polarization of the excitation. This can analytically be defined, considering the simplest exponential decay, as:

$$r(t) = (r_0 - r_\infty)e^{-\frac{t}{\varsigma}} + r_\infty, \tag{3}$$

where r_0 and r_∞ are the initial and final anisotropies, respectively, $\varsigma = \frac{\eta V}{RT}$ (for spherical molecules) is the depolarization rate constant dependent upon the temperature T, the viscosity of solution η, and the volume of excited species V. This temporal dependence of the emitted anisotropy corresponds to the instantaneous second-order parameter $P_2(\theta)$ (Equation (1)). The Perrin equation reveals the time dependence of rotational deactivation for a spherical rotor $\frac{r_0}{r} = 1 + \frac{\tau}{\varsigma}$, where τ is the fluorescence lifetime.

It is noteworthy that depolarization of emission from absorption is inherently related to the orientation of the corresponding absorption and emission transition dipole moments. Kasha's rule states that emission occurs from the single vibrationally relaxed lowest excited state of the corresponding spin multiplicity $S_1, S_2, \ldots$, while absorption/excitation TDM can have a different orientation with respect to the molecule axis in the Highest Occupied Molecular Orbital (HOMO) and the Lowest Unoccupied Molecular Orbital (LUMO) transition. The offset in the TDMs of absorbance and emission is an effective anisotropy, which is the largest for the parallel/co-linear. It is defined by $r_0 = \frac{2}{5} \times \frac{3\cos^2\beta - 1}{2}$, where the β is the angle between the TDMs of absorption and emission [26]. Hence, there is no anisotropy $r_0 = 0$ at the magic angle $\beta = 54.7^\circ$, the maximum $r_0 = 0.4$ at $\beta = 0^\circ$ and the minimum $r_0 = -0.2$ at $\beta = 90^\circ$.

The frequency-domain realization of FLIM is based on the temporal modulation of the excitation and on the synchronized detection of the phase-shifted signal applicable to liquid [27] as well as solid-state samples [28]. The frequency-domain approach was utilized to determine the lifetime from the phase ψ and modulation m of the fluorescence signal with an optical modulation frequency of 35 MHz, the lifetime (phase) $\tau_{(phase)} = \frac{1}{\omega}\tan(\psi)$, and lifetime (mod) $\tau_{(mod)} = \frac{1}{\omega}\sqrt{\frac{1}{m^2} - 1}$. The lifetime from the phase and the lifetime from the modulation can be used to determine the complexity of the system. When both lifetimes are equivalent, the system is a single lifetime system. When the lifetime from the phase is less than the lifetime from the modulation, the system is heterogeneous. And when the lifetime from the phase is larger than the lifetime from the modulation, the excited state reactions need to be considered. The typical phasor presentation: $B = m\cos\psi$ and $A = m\sin\psi$. The phasor method is well suited to measure fluorescence-lifetime changes due to dye–nanoparticle dye–environment interactions in solutions. To determine the anisotropy decay parameters, the FLIM-phasors under polarized-excitation and their perpendicular polarized detection conditions were measured and as described previously [29]. A model consisting of a free rotational mobile population and a hindered immobile population is assumed. The fraction hindered is given by $\frac{r_\infty}{r_0}$.

3. Results and Discussion

3.1. Optical Properties of 3D Sculptured Films

The width of porous channels in 3D sculptured coating of LaF_3 is 20–30 nm, and they are extending throughout the entire height of the surface structure as shown in Figure 1. The nanogaps were open on the surface in the sample without the 100 nm cap layer. This pattern of nanogaps made the effective surface tension different, and the surface energy was approximately twice as large along the slow axis when compared with the fast axis (aqueous solution of RhD6G droplet spreading is shown in Figure 2b).

The 3D sculptured coating has a form birefringence with extraordinary refractive index smaller than that of ordinary $n_e < n_o$, i.e., $\Delta n \equiv n_e - n_o < 0$. Figure 4 shows the transmittance spectrum $T(\lambda)$ for two linearly polarized beams along fast and slow axes. A clear separation of the interference pattern is discernible. The thickness of LaF_3 film is $d = 1.2$ µm, at $\lambda = 300$ nm, and the retardance $|\Delta n|d \approx 0.2\lambda$. This corresponds to high

birefringence $|\Delta n| = 0.05$. The birefringence is approximately three times lower in the long wavelength region at 800 nm.

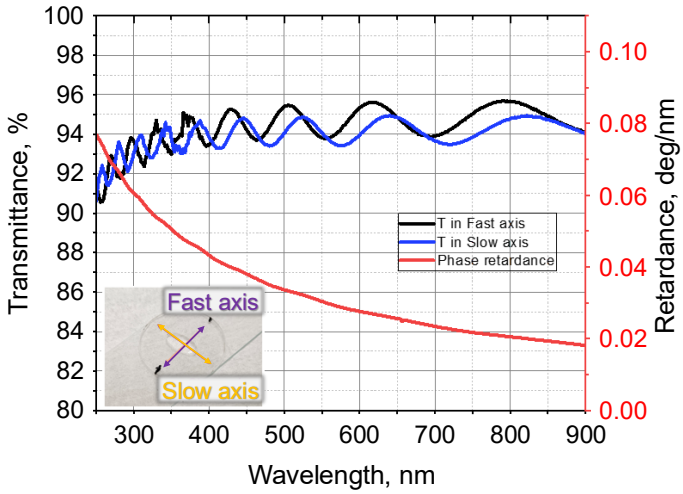

Figure 4. Transmittance along fast and slow axes and phase retardance $\Gamma_\lambda = \frac{360^\circ}{\lambda \Delta n}$ [degrees/nm] for linearly polarized beams. The inset shows the uncapped sample with a drop of RhD6G solution. For $\lambda = 300$ nm, the thickness of $\lambda/4$-plate $d = 360^\circ/\Gamma_\lambda = 1.5$ µm; where $\Gamma_\lambda = 0.06$ deg/nm.

The form birefringence depends on the volume fraction of material f and can be calculated from the known isotropic refractive index of LaF_3 for light's E-field oscillating along the extraordinary (along optical axis) and ordinary directions in the same way as for laser inscribed bulk nanogratings [30]:

$$n_e = \sqrt{\frac{n_1^2 n_2^2}{(1-f)n_2^2 + f n_1^2}}; \quad n_o = \sqrt{(1-f)n_1^2 + f n_2^2}, \tag{4}$$

where $n_{1,2}$ are the refractive indices of environment (air) and material (LaF_3), respectively. Figure 5 shows Equation (4) for two wavelengths of 300 nm and 800 nm. At low porosity ~93% (correspondingly high-volume fraction $f \approx 0.93$), a high birefringence $|\Delta n| \simeq 0.05$ can be achieved. This corresponds to nanogaps between nano-walls of LaF_3 only tens-of-nm wide in GLAD coatings investigated here. Useful virtue for application is the low wavelength dependence of form birefringence $\Delta n(\lambda) \simeq Const$. This analysis of form birefringence is only qualitatively applicable to the 3D sculptured GLAD coatings, which have a more complex structure. The experimentally measured retardance (Figure 4) and numerical simulations (Figure 5) are in agreement.

3.2. Fluorescence-Lifetime Imaging Microscopy

The phasor analysis is used to determine the lifetime τ (Figure 6). This approach involves first measuring the reference phasor (lifetime standard), then measuring the sample. Using the reference sample, instrumental corrections for phase lag and demodulation can be made, allowing finally the coordinates (A, B) of the measured sample to be obtained. The intersection point with the semicircle contains information about the lifetime (phase) of the sample with the background removed. The lifetime (phase) $\tau = \frac{A}{B\omega}$, where $\omega = 2\pi \times 35$ MHz is the modulation frequency. Phasors with the end point on the semicircle correspond to the single-exponential decay [31–34]. To determine the anisotropy decay parameters, the FLIM-phasors under polarized-excitation/orthogonal-polarized detection conditions were measured and analyzed as previously described [29]. Table 1 summarizes the results of the photophysical parameters of RhD6G dye as a droplet on the surface of uncapped 3D sculptured film (wet condition) and after absorption within

the structure (dry condition, which is ~4 h from droplet deposition). As a droplet on a non-porous substrate, the RhD6G has a lifetime close to 4 ns and exhibited a rotational correlation time of 0.2–0.3 ns, consistent with free rotation of the dye molecules in an aqueous environment [27]. These values were obtained for the RhD6G on a capped sample, when the dye (wet condition) was not permeating the porous GLAD film.

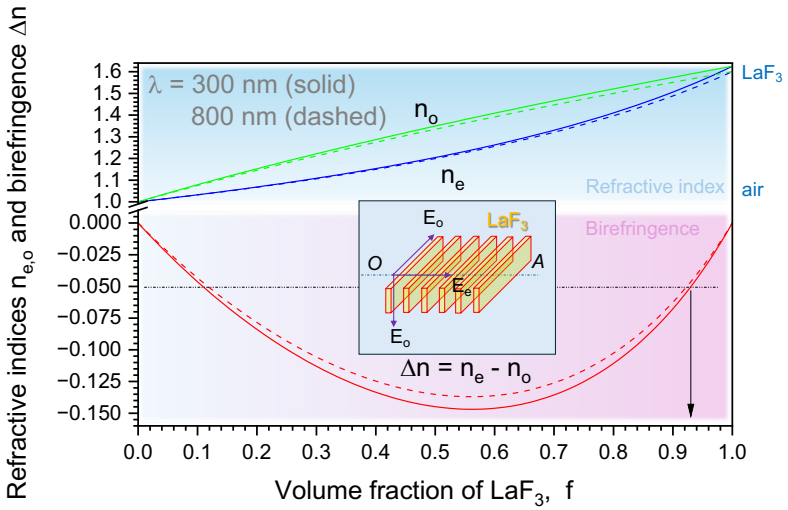

Figure 5. Form birefringence (negative) $\Delta n = n_e - n_o$ of LaF_3 3D grating with volume fraction of material $f = w/\Lambda$, where w is the width of the LaF_3 plane and Λ is the period. Arrow marks $f \approx 93\%$ volume fraction of $|\Delta n| = 0.05$. Refractive indices used: 1.6253 (at $\lambda = 300$ nm) and 1.6007 (800 nm). The inset shows the geometry of the form-birefringent structure.

After RhD6G droplets filled the nanogaps, quenching of the lifetime was observed, and the anisotropy decay exhibited complex dynamics (phasor ends are inside the semicircle in Figure 6). In the context of a free and immobilized model of dye molecules, in the permeated (and surface adsorbed) state, most of the dye was rotationally immobile, with the free state undergoing motion on the nanosecond time-scale. Of particular note is that the photophysics of the dye were orientation-independent in the wet state (as expected) but strongly dependent on the orientation after filling into the nanogaps of the permeable coating. A tentative explanation is that the dye–material interaction is orientation-dependent, with a greater extent of quenching and rotational hindrance in one direction relative to the orthogonal direction.

In the dried state (~4 h), the portion of rotationally hindered state was >57% (Table 1). The larger rotation hindrance ~89% was for the orientation along the gaps of the form-birefringent structure, i.e., along the ordinary axis (larger refractive index n_o) as compared with the extraordinary orientation (with index n_e). A possible explanation for this is that a larger portion of dye molecules has an energetic preference to align with the vertical walls of the LaF_3 nanoplanes. Apparently, a small portion of dye molecules is still able to undergo orientational changes (or re-emit after charge transfer to the neighboring molecules with different orientation [35]).

For the capped dried conditions, there was no fluorescence anisotropy on linear polarization of excitation at 470 nm along ordinary and extraordinary orientations, nor measurable rotation dephasing since molecules were immobilized in random orientation.

Lifetime quenching could be due to an increase in radiative rate due to refractive index increase (Strickler–Berg relationship) [36], but also possible non-radiative rate enhancement due to a change in environment (interaction with material). These mechanisms need further investigation. To elucidate light-intensity enhancement inside nanogaps of form-birefringent structures, a numerical study was carried out and is discussed next.

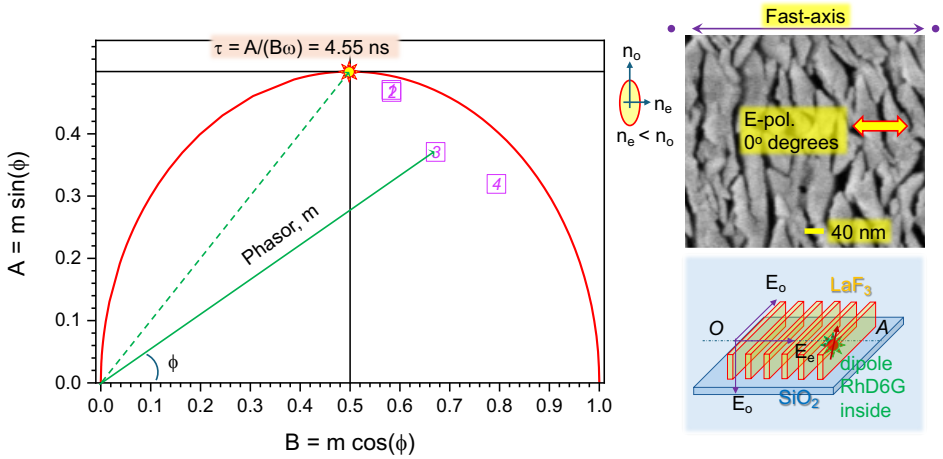

Figure 6. Phasor plot. Wet and dry RhD6G samples analyzed by FLIM method; the markers are sample No.# in Table 1. A total of 20 µL of solution was dropped on the surface of capped and non-capped LaF_3 samples. Optical modulation frequency $\nu = 35$ MHz; $\omega = 2\pi\nu$. Numerical aperture of the excitation/collection objective lens was $NA = 0.1$ and all the thickness 1.2 µm of LaF_3 coating was within the Rayleigh zone $z_R = \pi\omega_0^2/\lambda \simeq 55.1$ µm where the waist (radius) at the focus $\omega_0 = 0.61\lambda/NA = 2.87$ µm for $\lambda = 470$ nm. Dry condition corresponded to ~4 h after the droplet was placed on the surface of the sample. Insets show SEM image of top surface and schematics of form-birefringent structure.

Table 1. Rhodamine 6G fluorescence lifetime and time-resolved anisotropy decay parameters as a function of material condition and orientation. Lifetime (phase) is the lifetime calculated from the phase; lifetime (modulation) is the lifetime calculated from the modulation (optical modulation frequency was 35 MHz; see the phasor plot in Figure 6). Experimental uncertainty for lifetimes is ±0.1 ns.

Sample No.#: Film of LaF_3	Condition RhD6G 20 µL	Orientation H-Axis (0°) Slow-Axis	Lifetime (Phase) ϕ [ns]	Lifetime (Modulation) [ns]	Corr. Time [ns]	Fraction Hindered
1. uncapped	wet	0°	3.7	4.0	0.3	0
2. uncapped	wet	90°	3.6	4.0	0.2	0
3. uncapped	dry	0°	2.5	3.8	3.3	0.57
4. uncapped	dry	90°	1.8	2.8	0.6	0.89

3.3. Toy Model: Dipole in a Birefringent Cage

Numerical modeling by finite-difference time domain (FDTD) was carried out for a qualitative understanding of light excitation and dipole emission in a generic form-birefringent structure. This toy model has a gap of 20 nm and the same width of LaF_3 plains (duty cycle of 0.5 corresponding to the strongest form birefringence; Figure 5). While the model assumes an idealized periodic geometry with 10–20 nm gaps, the actual GLAD-induced porosity is stochastic, and the pore size distribution can vary from a few nanometers to tens of nanometers and increase with film thickness, as observed in the SEM images.

Using the dipole source in FDTD simulations, one can visualize light enhancement in close proximity (Figure 7). The dipole source is fundamentally different from a plane wave: it is not normalized to a fixed incident field amplitude, but instead injects power via a point electric dipole moment. As a result, the near-field $|E|^2$ can become very large and does not represent a normalized incident intensity. The effect of the structure on a dipole emitter is evaluated through the emitted power ratio (i.e., the Purcell factor or local density of states (LDOS) enhancement) by comparing the dipole-emitted power with and

without the structure, rather than using field-intensity monitors. The Purcell framework allows for the interpretation of the orientation-dependent lifetime shortening within the anisotropic nanogaps, as observed experimentally. The field maps are therefore used only to illustrate the spatial redistribution of the electromagnetic field and do not represent emission enhancement.

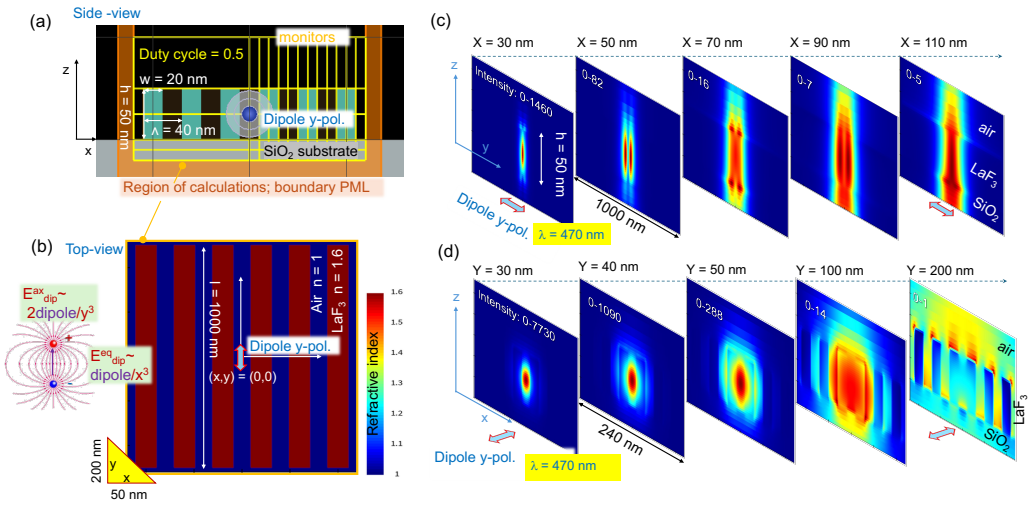

Figure 7. Toy-model . FDTD simulation of dipole field inside form-birefringent region. (**a**) Side-view scene with parameters: $\Lambda = 40$ nm period, dipole location is at $(x, y) = (0, 0)$ and middle of the structure at $z = 25$ nm. (**b**) Top-view of refractive index monitor over the entire calculation region with perfectly matched layer (PML) conditions. The inset shows the dipole, and its E-fields on axis and equator. (**c**) E-field enhancement on (Y, Z)-plane at different X-position. (**d**) E-field enhancement as the emitted power ratio on the (X, Z)-plane at different Y-positions. The enhancement range of the cold-hot maps is shown as intensity in (**c**,**d**).

For visualization of field enhancement, a $\lambda = 470$ nm dipole was placed at the center of the 20-nm-wide groove of the form-birefringent structure at mid-height of 25 nm. This $\lambda = 470$ nm is the wavelength of RhD6G excitation; however, the qualitatively same result of field enhancement (emitted power ratio) was also for the Stokes-shifted fluorescence at ~570 nm. Figure 7c,d enhancement or Purcell factor maps visualize a very fast decay of enhancement from the position of a y-polarized dipole placed at $(x, y, z) = (0, 0, 25)$ nm. Enhancement decay along the x-direction (the equatorial direction of y-polarized dipole) is approximately by one order of magnitude in every next well of the structure (Figure 7c). In the direction along the dipole axis (along the y-direction), a similar very fast decay of enhancement was observed. The enhancement was well localized inside the center groove where the dipole was placed (Figure 7c). This is consistent with the E-field decay from a dipole in a free space which has the axial and equatorial distributions: $E^{ax}_{dip} \sim 2 \times dipole/y^3$ and $E^{eq}_{dip} \sim dipole/x^3$, both polarized along the dipole, i.e., y-polarized where the dipole momentum is defined by the two charges $\pm q$ separated by y_d as $\mathbf{dipole} = q\mathbf{y_d}$ with dipole orientation from negative to positive $- \rightarrow +$. Hence, the local intensity, which is E^2, has a very steep decay $1/x^6$ (equatorial) or $1/y^6$ (axial) and has a smaller amplitude in the equatorial direction by a factor of 2^2 as compared with the axial (Figure 7b). This scaling is for a dipole in free space, while the addition of the structure and high refractive index walls in close proximity facilitates further localization of emission inside the groove via a slot-wave-guiding mechanism. The Figure 7c,d shows enhancement (the emitted power ratio) for the total field, which has a more complex polarization pattern if separated into the constituent contributions $E^2 = E^2_x + E^2_y + E^2_z$ and it is always available in the FDTD field monitors.

Next, let us estimate the field enhancement for the dipole in the form-birefringent structure at the perpendicular direction (along n_e fast axis). Figure 8 shows E-field enhancement maps (proportional to the Purcell's factor) along the fast- and slow axis (x- and y-axis, respectively). Strong light localization inside the gap is evident, as well as strong dependence of intensity decay from the dipole source. As expected, stronger light localization inside the nanogap was for the dipole along the fast axis n_e (Figure 8) as compared with the slow axis n_o (Figure 7). The higher light localization inside nanogaps for the E-field (dipole or plane-wave source) oriented perpendicular to the interface is based on the boundary condition for the normal component of displacement $D = \varepsilon_0 \varepsilon E$, where ε_0 is the permittivity of free space and $\varepsilon \equiv n^2$ is the permittivity of the material. At the interface LaF_3-air(gap), $D_n^{\mathrm{LaF_3}} = D_n^{\mathrm{air}}$ or $E_n^{\mathrm{LaF_3}} \times n_{\mathrm{LaF_3}}^2 = E_n^{air} \times n_{air}^2$. For intensity in air nanogap, this reads $|E_n^{air}|^2 = [\frac{n_{\mathrm{LaF_3}}}{n_{air}}]^4 \times |E_n^{\mathrm{LaF_3}}|^2 \equiv n_{\mathrm{LaF_3}}^4 |E_n^{\mathrm{LaF_3}}|^2$. The intensity enhancement by a factor $1.6^4 \simeq 6.6$ times is expected for $n_{\mathrm{LaF_3}} \simeq 1.6$. The tangential components of the E-field are equal on both sides of the interface (no enhancement); see Appendix A for plane-wave illumination of the same structure as in Figures 7 and 8. Redistribution of light preferentially into nanogaps can explain the higher damage threshold of 3D sculptured coatings in high intensity laser beams [6].

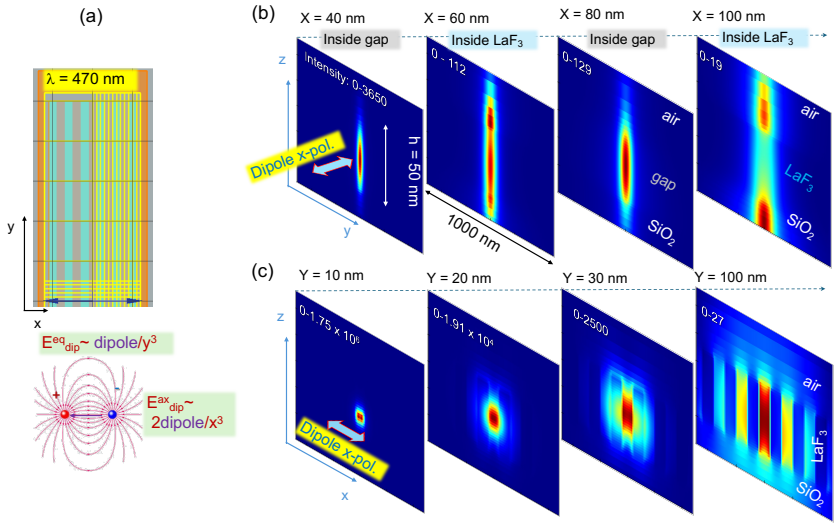

Figure 8. Toy-model. FDTD simulation of dipole field inside form-birefringent region with dipole along the n_e (fast axis). (**a**) Top-view scene with parameters: $\Lambda = 40$ nm period, dipole location is at $(x, y) = (0, 0)$ and middle of the structure at $z = 25$ nm. The perfectly matched layer (PML) conditions were used with different-sized meshing for high resolution. Bottom-inset shows the dipole, and its E-fields on axis and equator. (**b**) E-field enhancement on (Y, Z)-plane at different X-position. (**c**) E-field enhancement as the emitted power ratio on the (X, Z)-plane at different Y-positions. The enhancement range of the cold-hot maps is shown as intensity in (**b**,**c**).

Analysis of FDTD results for a dye-dipole emitting inside the form-birefringent structure predicts a stronger fluorescence (shorter lifetime due to the Purcell enhancement) in the extraordinary orientation along the n_e (fast axis) due to larger E-field localization inside nanogaps. However, the observed tendency in experiments for the dried sample (90° in Table 1) is that a shorter fluorescence lifetime (if it is due to the Purcell enhancement) is for the excitation oriented along the slow axis n_o-direction. This could be explained by the preferential alignment of flat RhD6G molecules along the walls of the form-birefringent GLAD structure. For such orientation, a stronger E-field perpendicular to the walls does not excite dyes (oriented along the walls). Further studies are needed to test this hypothesis when different form-birefringent structures are filled with the dye solution. Separation of orientation due to absorbing dipoles induces dichroism, which can be distinguished from

the orientation of the birefringent host as demonstrated earlier [37] and is made available as a freeware data analysis tool [38]. This four-polarization analysis of orientation has inherent super-resolution capability [39,40].

4. Conclusions and Outlook

Rhodamine 6G aqueous solution dropped onto form-birefringent 3D sculptured GLAD coatings showed the absence of rotational anisotropy of fluorescence, similarly as in solution. The shortening of fluorescence/photoluminescence lifetime by ∼10% was observed from the dye-permeated (in liquid form) structure; however, there was no rotational hindrance of dye molecules. When dried, a strong rotational hindrance 89% was observed for the orientation along the ordinary optical axis (slow-axis), and the hindrance was smaller 57% for the extraordinary direction (fast axis). Light-intensity distribution inside a nano-structure with a form birefringence was numerically modeled using plane-wave illumination and a dipole source. Nanoscale localization of light intensity due to dipole nature $I \sim 1/r^6$ and boundary conditions for E-field allows efficient energy deposition inside the region of lower refractive index (nanogaps). While direct quantification of photostability and the decay process was not measured, the observed reduction in fluorescence lifetime and the significant rotational hindrance support the hypothesis that these 3D coatings can enhance dye photostability.

Author Contributions: Conceptualization, L.G., S.J., and A.H.A.C.; methodology, L.G., S.J., and A.H.A.C.; software, H.M., and A.H.A.C.; validation, All authors; formal analysis, All authors; investigation, L.G., and A.H.A.C.; resources, L.G., S.J., and A.H.A.C.; data curation, L.G., S.J., and A.H.A.C.; writing—original draft preparation, L.G., H.-H.H., S.J., and A.H.A.C.; writing—review and editing, All authors; visualization, L.G., H.-H.H., H.M., S.J., and A.H.A.C.; supervision, L.G., J.W.M.C., S.J., and A.H.A.C. All authors have read and agreed to the published version of the manuscript.

Funding: L.G. received funding from the Research Council of Lithuania (LMTLT), agreement No. S-PD-24-94. S.J. acknowledges support via the ARC DP240103231 grant.

Data Availability Statement: The original contributions presented in this study are included in the article. Further inquiries can be directed to the corresponding authors.

Acknowledgments: H.-H.H. is grateful for a research stay at the Laser Research Center, Vilnius University, in 2025. We are grateful to Jimmy Wales for continuous support. S.J. is grateful to the Nanotechnology Ambassador program at the MCN-ANFF node in 2024-25.

Conflicts of Interest: The authors declare no conflicts of interest.

Appendix A

Figure A1 shows FDTD simulations for plane-wave incidence over the 1000 × 240 nm^2 area of form-birefringent pattern of LaF_3 nanoplanes (50-nm-tall), 20-nm-wide, and with a duty cycle of 0.5 (20-nm-gap of air between planes) on SiO_2 slab. Polarization of incident light is along the fast and slow axes of the structure at two wavelengths, 470 nm and 570 nm. Those wavelengths correspond to the excitation of RhD6G and its emission, respectively. Field monitors were set parallel and perpendicular to the E-polarization. It is noteworthy that there was a 10 nm wide rim without any structure around the entire grating pattern. This caused some periodicity in the pattern (the (YZ)-plane at $x = 0$), which would not be expected for the periodic boundary condition. There was a minor difference between light-intensity enhancement maps for both wavelengths. When the E-field was along the fast axis (x-axis), there was a strong enhancement in the air gaps. In those gaps, the RhD6G solution was filled in experiments. This is due to the boundary condition discussed in the main text. Nano-porous ordered structures could find applications in micro-lasers, e.g., opals or inverted opals showed lasing when filled with rhodamine solution [41].

Figure A2 shows a columnar structure made of birefringent columnar pillars. It is evident that the E-field is more enhanced between two pillars in the direction of the higher refractive index (along the y-axis). Illumination of the structure was a plane wave.

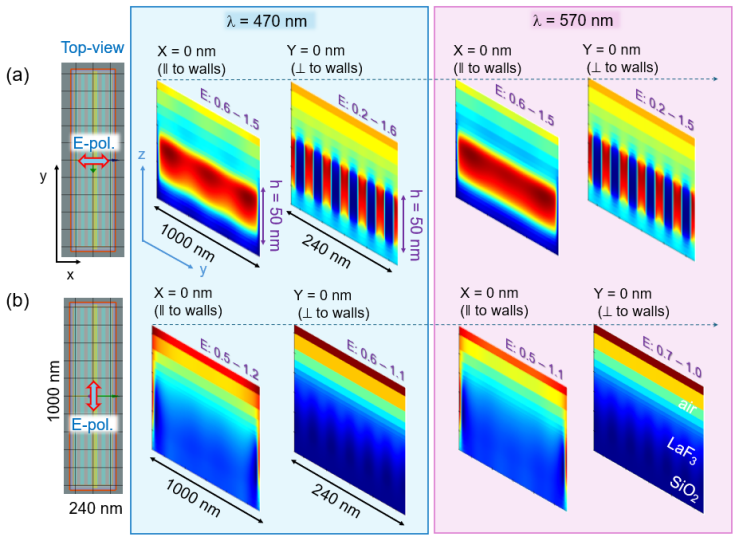

Figure A1. Toy-model. FDTD simulation of plane-wave illumination of the form-birefringent structure at two perpendicular polarizations along the fast axis (**a**) and slow axis (**b**) (the same structure was used in Figures 7 and 8). The periodic boundary conditions (PBC) were used with different-sized meshing for high resolution. Incident E-field is normalized $|E| = 1$.

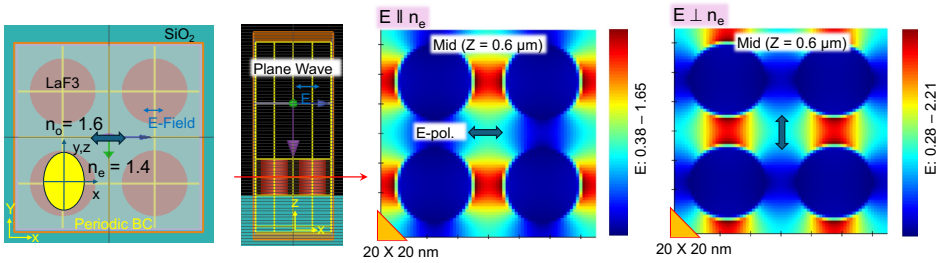

Figure A2. Birefringent structure model: columnar pillars of 1.2 μm have inherent birefringence $n_e < n_o$ (1.4 < 1.6), similar to form-birefringent plane structures studied here. FDTD simulation of plane-wave illumination of the birefringent structure with E-field enhancement maps. The periodic boundary conditions (PBC) were used with different-sized meshing for high resolution. Incident E-field is normalized $|E| = 1$.

References

1. Robbie, K.; Brett, M.J. Sculptured thin films and glancing angle deposition: Growth mechanics and applications. *J. Vac. Sci. Technol. A Vac. Surfaces Films* **1997**, *15*, 1460–1465. [CrossRef]
2. Hawkeye, M.M.; Brett, M.J. Glancing angle deposition: Fabrication, properties, and applications of micro- and nanostructured thin films. *J. Vac. Sci. Technol. A Vac. Surfaces Films* **2007**, *25*, 1317–1335. [CrossRef]
3. Robbie, K.; Brett, M.J.; Lakhtakia, A. Chiral sculptured thin films. *Nature* **1996**, *384*, 616–616. [CrossRef]
4. Vick, D.; Friedrich, L.; Dew, S.; Brett, M.; Robbie, K.; Seto, M.; Smy, T. Self-shadowing and surface diffusion effects in obliquely deposited thin films. *Thin Solid Films* **1999**, *339*, 88–94. [CrossRef]
5. Messier, R.; Giri, A.P.; Roy, R.A. Revised structure zone model for thin film physical structure. *J. Vac. Sci. Technol. A Vac. Surfaces Films* **1984**, *2*, 500–503. [CrossRef]
6. Grinevičiūtė, L.; Andrulevičius, M.; Melninkaitis, A.; Buzelis, R.; Selskis, A.; Lazauskas, A.; Tolenis, T. Highly Resistant Zero-Order Waveplates Based on All-Silica Multilayer Coatings. *Phys. Status Solidi (A)* **2017**, *214*, 1700764. [CrossRef]
7. MacNally, S.; Smith, C.; Spaulding, J.; Foster, J.; Oliver, J.B. Glancing-Angle-Deposited Silica Films for Ultraviolet Wave Plates. *Appl. Opt.* **2020**, *59*, A155. [CrossRef] [PubMed]
8. Grineviciute, L.; Tolenis, T.; Ryu, M.; Moein, T.; Ng, S.H.; Katkus, T.; Maksimovic, J.; Drazdys, R.; Morikawa, J.; Juodkazis, S. Releasable Micro-Waveplates. *arXiv* **2019**, arXiv:1907.05485 [CrossRef]

9. Grineviciute, L.; Nikitina, J.; Babayigit, C.; Staliunas, K. Fano-like resonances in nanostructured thin films for spatial filtering. *Appl. Phys. Lett.* **2021**, *118*, 131114. [CrossRef]
10. Lukosiunas, I.; Grineviciute, L.; Nikitina, J.; Gailevicius, D.; Staliunas, K. Extremely narrow sharply peaked resonances at the edge of the continuum. *Phys. Rev. A* **2023**, *107*, L061501. [CrossRef]
11. Grineviciute, L.; Moein, T.; Han, M.; Ng, S.H.; Anand, V.; Katkus, T.; Ryu, M.; Morikawa, J.; Tobin, M.J.; Vongsvivut, J.; et al. Optical anisotropy of glancing angle deposited thin films on nano-patterned substrates. *Opt. Mater. Express* **2022**, *12*, 1281–1290. [CrossRef]
12. Grineviciute, L.; Ng, S.H.; Han, M.; Moein, T.; Anand, V.; Katkus, T.; Ryu, M.; Morikawa, J.; Tobin, M.J.; Vongsvivut, J.; et al. Anisotropy of 3D Columnar Coatings in Mid-Infrared Spectral Range. *Nanomaterials* **2021**, *11*, 3247. [CrossRef]
13. Bairagi, S.; Järrendahl, K.; Eriksson, F.; Hultman, L.; Birch, J.; Hsiao, C.L. Glancing Angle Deposition and Growth Mechanism of Inclined AlN Nanostructures Using Reactive Magnetron Sputtering. *Coatings* **2020**, *10*, 768. [CrossRef]
14. Mao, L.; Zhu, S.; Ma, J.; Shi, D.; Chen, Y.; Chen, Z.; Yin, C.; Li, Y.; Zhang, D. Superior H_2 production by hydrophilic ultrafine Ta_2O_5 engineered covalently on graphene. *Nanotechnology* **2014**, *25*, 215401. [CrossRef] [PubMed]
15. Kapil, V.; Schran, C.; Zen, A.; Chen, J.; Pickard, C.J.; Michaelides, A. The First-Principles Phase Diagram of Monolayer Nanoconfined Water. *Nature* **2022**, *609*, 512–516. [CrossRef]
16. Surwade, S.P.; Smirnov, S.N.; Vlassiouk, I.V.; Unocic, R.R.; Veith, G.M.; Dai, S.; Mahurin, S.M. Water Desalination Using Nanoporous Single-Layer Graphene. *Nat. Nanotechnol.* **2015**, *10*, 459–464. [CrossRef]
17. Wang, Y.; Tang, F.; Yu, X.; Chiang, K.Y.; Yu, C.C.; Ohto, T.; Chen, Y.; Nagata, Y.; Bonn, M. Interfaces Govern the Structure of Angstrom-Scale Confined Water Solutions. *Nat. Commun.* **2025**, *16*, 7288. [CrossRef] [PubMed]
18. Würth, C.; González, M.G.; Niessner, R.; Panne, U.; Haisch, C.; Genger, U.R. Determination of the Absolute Fluorescence Quantum Yield of Rhodamine 6G with Optical and Photoacoustic Methods – Providing the Basis for Fluorescence Quantum Yield Standards. *Talanta* **2012**, *90*, 30–37. [CrossRef]
19. Penzkofer, A.; Leupacher, W. Fluorescence behaviour of highly concentrated rhodamine 6G solutions. *J. Lumin.* **1987**, *37*, 61–72. [CrossRef]
20. Fischer, M.; Georges, J. Fluorescence quantum yield of rhodamine 6G in ethanol as a function of concentration using thermal lens spectrometry. *Chem. Phys. Lett.* **1996**, *260*, 115–118. [CrossRef]
21. Penzkofer, A.; Wiedmann, J. Orientation of Transition Dipole Moments of Rhodamine 6G Determined by Excited State Absorption. *Opt. Commun.* **1980**, *35*, 81–86. [CrossRef]
22. Doveiko, D.; Kubiak-Ossowska, K.; Chen, Y. Impact of the Crystal Structure of Silica Nanoparticles on Rhodamine 6G Adsorption: A Molecular Dynamics Study. *ACS Omega* **2024**, *9*, 4123–4136. [CrossRef]
23. Trenkmann, I.; Bok, S.; Korampally, V.R.; Gangopadhyay, S.; Graaf, H.; Von Borczyskowski, C. Counting single Rhodamine 6G dye molecules in organosilicate nanoparticles. *Chem. Phys.* **2012**, *406*, 41–46. [CrossRef]
24. Astrauskyte, D.; Slipkauskas, M.; Tumenas, S.; Selskiene, A.; Ramalis, L.; Grineviciute, L. Performance and stability evaluation of LaF3 thin-film waveplates for high-power 266 nm laser applications. *Nanoscale* 2026, *in press*. [CrossRef]
25. Torrado, B.; Pannunzio, B.; Malacrida, L.; Digman, M.A. Fluorescence Lifetime Imaging Microscopy. *Nat. Rev. Methods Prim.* **2024**, *4*, 80. [CrossRef]
26. Dickinson, F. Chapter 5 Fluorescence Anisotropy & Applications of Fluorescence. Available online: https://chemfd.github.io/AOS/ch-fluorother.html (accessed on 18 December 2025).
27. Kubiliūtė, R.; Maximova, K.; Lajevardipour, A.; Yong, J.; Hartley, J.; Mohsin, A.; Blandin, P.; Chon, J.; Sentis, M.; Stoddart, P.; et al. Ultra-pure, water-dispersed Au nanoparticles produced by femtosecond laser ablation and fragmentation. *Int. J. Nanomed.* **2013**, *8*, 2601–2611. [CrossRef]
28. de Jong, C.J.; Lajevardipour, A.; Gecevičius, M.; Beresna, M.; Gervinskas, G.; Kazansky, P.G.; Bellouard, Y.; Clayton, A.H.A.; Juodkazis, S. Deep-UV fluorescence lifetime imaging microscopy. *Photon. Res.* **2015**, *3*, 283–288. [CrossRef]
29. Kozer, N.; Clayton, A.H.A. Analysis of Complex Anisotropy Decays from Single-Frequency Polarized-Phasor Ellipse Plots. *Methods Appl. Fluoresc.* **2016**, *4*, 024005. [CrossRef]
30. Buividas, R.; Mikutis, M.; Juodkazis, S. Surface and bulk structuring of materials by ripples with long and short laser pulses: Recent advances. *Prog. Quantum Electron.* **2014**, *38*, 119–156. [CrossRef]
31. Jameson, D.M.; Gratton, E.; Hall, R.D. The Measurement and Analysis of Heterogeneous Emissions by Multifrequency Phase and Modulation Fluorometry. *Appl. Spectrosc. Rev.* **1984**, *20*, 55–106. [CrossRef]
32. Clayton, A.H.A.; Hanley, Q.S.; Verveer, P.J. Graphical Representation and Multicomponent Analysis of Single-frequency Fluorescence Lifetime Imaging Microscopy Data. *J. Microsc.* **2004**, *213*, 1–5. [CrossRef] [PubMed]
33. Redford, G.I.; Clegg, R.M. Polar Plot Representation for Frequency-Domain Analysis of Fluorescence Lifetimes. *J. Fluoresc.* **2005**, *15*, 805–815. [CrossRef]
34. Digman, M.A.; Caiolfa, V.R.; Zamai, M.; Gratton, E. The Phasor Approach to Fluorescence Lifetime Imaging Analysis. *Biophys. J.* **2008**, *94*, L14–L16. [CrossRef]

35. López, S.G.; Worringer, G.; Rodríguez, H.B.; San Román, E. Trapping of Rhodamine 6G excitation energy on cellulose microparticles. *Phys. Chem. Chem. Phys.* **2010**, *12*, 2246–2253. [CrossRef]
36. Toptygin, D. Effects of the Solvent Refractive Index and Its Dispersion on the Radiative Decay Rate and Extinction Coefficient of a Fluorescent Solute. *J. Fluoresc.* **2003**, *13*, 201–219. [CrossRef]
37. Honda, R.; Ryu, M.; Balčytis, A.; Vongsvivut, J.; Tobin, M.J.; Juodkazis, S.; Morikawa, J. Paracetamol micro-structure analysis by optical mapping. *Appl. Surf. Sci.* **2019**, *473*, 127–132. [CrossRef]
38. Gassner, C.; Vongsvivut, J.; Ryu, M.; Ng, S.H.; Toplak, M.; Anand, V.; Takkalkar, P.; Fac, M.L.; Sims, N.A.; Wood, B.R.; et al. Bridging Spectroscopy and Advanced Molecular Orientation Analysis with New 4+ Angle Polarization Toolbox in Quasar. *Comput. Biol. Med.* **2025**, *196*, 110573. [CrossRef]
39. Honda, R.; Ryu, M.; Moritake, M.; Balčytis, A.; Mizeikis, V.; Vongsvivut, J.; Tobin, M.J.; Appadoo, D.; Li, J.L.; Ng, S.H.; et al. Infrared Polariscopy Imaging of Linear Polymeric Patterns with a Focal Plane Array. *Nanomaterials* **2019**, *9*, 732. [CrossRef] [PubMed]
40. Ryu, M.; Huang, H.H.; Vongsvivut, J.; Ng, S.H.; Dumbrytė, I.; Narbutis, D.; Malinauskas, M.; Juodkazis, S.; Morikawa, J. Anisotropy Analysis of Bamboo and Tooth Using 4-Angle Polarization Micro-Spectroscopy. *Nano Select* **2025**, e70099. [CrossRef]
41. Nishijima, Y.; Juodkazis, S. Optical Characterization and Lasing in Three-Dimensional Opal-Structures. *Front. Mater.* **2015**, *2*, 49. [CrossRef]